Available online at www.sciencedirect.com

SCIENCE DIRECT®

Microelectronic Engineering 75 (2004) 12–23

MICROELECTRONIC ENGINEERING

www.elsevier.com/locate/mee

High strain behavior of composite thin film piezoelectric membranes

I. Demir, A.L. Olson, J.L. Skinner, C.D. Richards, R.F. Richards, D.F. Bahr *

School of Mechanical and Materials Engineering, Washington State University, P.O. Box 642920 Pullman, WA 99164-2920, USA

Received 31 July 2003; received in revised form 19 September 2003; accepted 24 October 2003
Available online 27 February 2004

Abstract

The behavior of thin-film piezoelectric membranes at high deflections and strains for use as generators is examined. Experiments are conducted with a bulge tester to obtain pressure–deflection relationships, residual stresses, and electrical output characteristics of the piezoelectric membranes. A model is developed using an energy minimization technique. The experimental results are compared to the modeled results. Experimental results have shown that increasing PZT thickness and the Ti ratio of the PZT chemistry lead to increased power output for a given deflection. The presence of tensile residual stress in the composite structure can result in lower deflections for a given force and thus impact electrical output. Increasing the Ti ratio leads to a reduction in residual stress.
© 2004 Elsevier B.V. All rights reserved.

Keywords: PZT; Residual stress; MEMS

1. Introduction

The need for miniaturized power sources for MEMS and microelectronics devices has long been recognized. Among the micro-scale concepts to generate electrical power using now being explored are fuel cells, static heat engines and dynamic heat engines. Recent work at Washington State University has been directed at the design of a micro heat engine which incorporates a thin-film piezoelectric membrane generator [1]. The micro engine is an external-combustion dynamic heat engine that produces electrical power when the flexible piezoelectric membrane is driven by the periodic expansion and compression of a two-phase working fluid. The pressure pulse applied by the two-phase working fluid causes the piezoelectric membrane to flex out, straining the piezoelectric ceramic. This straining of the piezoelectric material causes the film to become thinner, due to Poisson's effect, and results in an electric potential across the electrodes. Since the pressure pulse is periodic, the membrane oscillates and produces an alternating current.

Lead zirconate titanate ($PbZr_xTi_{1-x}O_3$, PZT), a piezoelectric oxide, is used in this device. PZT, a

* Corresponding author. Tel.: +1-509-335-8523; fax: +1-509-335-4662.
E-mail address: bahr@mail.wsu.edu (D.F. Bahr).

0167-9317/$ - see front matter © 2004 Elsevier B.V. All rights reserved.
doi:10.1016/j.mee.2003.10.007

Nomenclature

A	area, m^2	S_2	applied strain in 2 direction
a	membrane sidelength, m	T	kinetic energy, J
a_i	constant	t	thickness of membrane, m
b_i	constant	U	strain energy density function
C	constant	u	deflection in x-direction, m
c_i	constant	V	volume, m^3
d	applied stress, N/m^2	v	deflection in y-direction, m
D_3	electric displacement in three direction	W	work, N m
d_{31}	piezoelectric charge coefficient, C/N	w	deflection out of plane, m
E	Young's modulus, Pa	w_0	midpoint deflection of membrane, m
e	strain	x	cardinal direction
e_{31}	strain based piezoelectric coefficient, C/m^2	y	cardinal direction
FOM	figure of merit	δ	deflection, m
g_{31}	piezoelectric charge coefficient, m^2/C	$\tan\delta$	dielectric loss coefficient
h_{31}	field based piezoelectric coefficient	ε_{ij}	strain tensor
H	electrical enthalpy density	ε^T	dielectric constant
k	spring constant, N/m	ϕ_i	base function
L	Lagrangian	φ_i	base function
M	biaxial modulus, Pa	v	Poisson's ratio
m_o	bending moment caused by residual stress, N m	λ	wavelength, m
p	pressure, Pa	Π	total potential energy, J
S	applied biaxial strain	σ_0	residual stress, Pa
S_1	applied strain in 1 direction	σ_{ij}	stress tensor
		Ψ_i	base function

preferred material in many MEMS applications due to its high piezoelectric and electromechanical coupling coefficients [2] is widely used in sensing and actuating MEMS applications [3]. The structure of the thin-film piezoelectric membrane generator chosen for the micro engine is a simple two-dimensional sandwich structure similar to that used for pressure transducers and ultrasonic transducers [4].

Although the design and structure are similar to that of other devices, the thin-film PZT membranes used in this work are operated at very high strains (>0.05%) for extended periods of time to produce useable power. Typically strains in PZT transducers are less than 0.05%. Thus, characterization of the behavior of the thin-films in this relatively high strain regime is required. Both electrical and mechanical properties of the films are important to the application of power generation. Although mechanical test data on silicon for MEMS [5,6] and PZT are available [7], little is available for composite structures. Hardness and adhesion are measured via nanoindentation [8] on PZT, but these measurements do not probe the properties of the material in a manner similar to the service environment. In service the films will flex in tension, whereas during nanoindentation testing the primary mode of deformation is compression and shear. Studies of metal ceramic interfaces show that cyclic stresses can substantially differ than those measured in either bulk material [9]. Thus electromechanical characterization of the composite thin-film PZT membranes is required.

In this paper the behavior of the thin film piezoelectric membranes at high deflections and strains is examined. Experiments are conducted to obtain pressure–deflection relationships, residual stresses, and electrical output characteristics of the piezoelectric membranes. A model is developed using an

energy minimization technique. The experimental results are compared to the modeled results. The model is then used to explore the effects of residual stress.

2. Experimental procedures

2.1. Thin-film PZT membrane fabrication

The form of the thin-film piezoelectric membrane generator is a simple two-dimensional sandwich structure similar to that found in MEMS pressure and ultrasonic transducers. Fig. 1 shows a cross section of the piezoelectric membrane, which consists of a silicon membrane, a bottom platinum electrode, a thin-film of the piezoelectric ceramic PZT and a top gold electrode. Piezoelectric membranes are fabricated by first bulk micromachining silicon membranes and then depositing a thin-film generator stack on the membranes.

Membranes for the generators are bulk micromachined in (1 0 0) silicon wafers. Oxide layers are grown on both sides of the wafer through a wet thermal process. The oxide on the front side of the wafer is etched away and boron diffused into the silicon to form an etch stop. The boron skin and the back-side oxide layer are then stripped away using BOE (buffered oxide etchant). A layer of low temperature oxide is then grown on both sides of the wafer. The oxide serves two purposes: it acts as a barrier layer to electrically isolate the boron-doped side of the wafer and as an etch stop for the anisotropic etch. Photolithography is used to define the square membrane geometry on the back side of the wafer using a negative photoresist. A subsequent anisotropic wet etch in EDP (ethylene–diamine–pyrocatechol) creates square pyramidal cavities in the silicon wafer. The boron etch stop controls resulting membranes thicknesses. Currently membranes with thicknesses between 1.0 and 3.0 μm are fabricated. Membrane side lengths range from 1.45 to 4.0 mm.

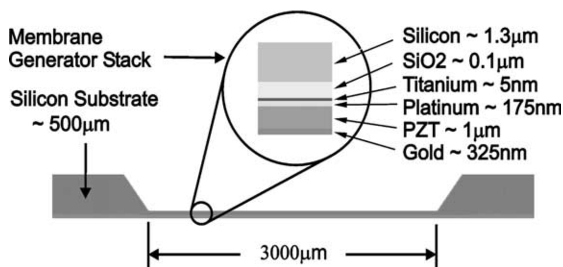

Fig. 1. Cross section of thin-film PZT membrane generator.

Thin-film generator stacks are fabricated on the membranes on the front side of the wafer. A common bottom electrode is formed by depositing 12 nm of titanium followed by 175 nm of platinum using DC magnetron sputtering and then annealing at 650 °C for 10 min. A thin film of piezoelectric ceramic is deposited on the electrode by spin coating the wafer with a PZT solution using a sol–gel process [10]. Two Zr:Ti ratios are used, 40:60 and 52:48. Pyrolosis at 375 °C for 2 min is performed for individual layers. Every layer adds about 90 nm to the film. After every third layer, the amorphous film is crystallized at 700 °C for 10 min. The final PZT film thickness has been varied from 250 nm to 2 μm.

Top electrodes are formed by sputtering 12 nm of titanium/tungsten and then 300 nm of gold on top of the PZT thin film. The geometry of the electrode pads and electrical leads are defined by photolithography. In some cases, the PZT thin film is etched away at locations of high strain at the membrane shoulders. Upon completion of fabrication, the piezoelectric ceramic is poled by applying 120 kV/cm parallel to the direction of measurement.

Film thicknesses were determined by either profilometry during fabrication or by cross sectioning the membranes and imaging in a LEO 982 field emission scanning electron microscope (FE-SEM). Residual stresses of membranes were found using pressure–deflection tests.

2.2. Diagnostics

In order to characterize the performance of a piezoelectric membrane, both the means to apply controlled static and dynamic pressures to the generator and the diagnostics to monitor the behavior of the generator are required. To this end, a generator characterization facility was constructed. The facility, described in detail in [11], consists of a bulge tester to apply either static or cyclic pressure pulses, an interferometer to measure membrane

deflection in real time, an oscilloscope to monitor the electrical output of the generator, and control/timing electronics to coordinate all functions. A block diagram of the facility is shown in Fig. 2.

The bulge tester may be used to apply either static pressures or dynamic pressure waves to a piezoelectric membrane. Static pressures up to 700 kPa may be applied by turning a micrometer against the steel diaphragm. Dynamic pressures may be applied by activating a piezoelectric actuator brought in contact with the steel diaphragm. A pressure sensor is mounted on the sidewall of the cavity. Periodic pressure waves of arbitrary functional form can be applied by driving the actuator with voltages generated by a function generator. Operated in this way, the actuator is capable of driving the bulge tester with arbitrarily shaped pressure pulses with maximum peak-to-peak pressures of 80 kPa at frequencies up to 2500 Hz.

Membrane deflection is measured using the interferometer depicted in Fig. 2. The light source is a pulsed Nd:YAG laser with a wavelength of $\lambda = 532$ nm and a 7 ns pulse width. A long working-distance microscope images the interference fringe pattern onto the 1024×1024 digital camera. Images are captured and recorded via a frame grabber in the computer. Interferograms may be captured at any point during periodic motion of the piezoelectric membrane to produce a complete picture of the membrane deflection at every point in the cycle. At the same time, the bulge tester dynamic pressure and the piezoelectric membrane output voltage may be viewed in real time on the oscilloscope and saved for later analysis.

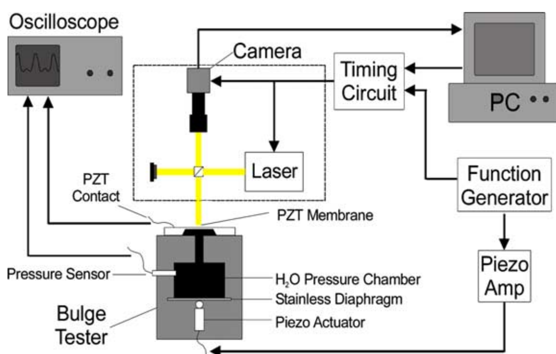

Fig. 2. Schematic of characterization facility.

3. Results and discussion

3.1. Characterization of electrical output

Important parameters to the output voltage produced by a piezoelectric membrane are the thickness of the PZT layer and the strain generated in the PZT layer during maximum membrane deflection. Fig. 3 illustrates these dependencies. In the figure, peak-to-peak open-circuit voltages are plotted against the tensile strain experienced by the PZT layer during maximum piezoelectric membrane deflection. Measurements are given for membrane generators with PZT layer thicknesses ranging from 0.8 to 1.6 μm, undergoing strains up to 0.1% on 2 μm thick Si membranes. Piezoelectric membrane output voltage increases linearly both with PZT layer thickness and with PZT maximum strain.

Based on the deflection and shape measured from the interferometer, the maximum applied biaxial strain, S, in these square membranes of side length a, can be calculated by [12]:

$$S = C\delta^2/a^2, \qquad (1)$$

where $C = 0.883$ at the membrane center, for a Poisson's ratio of 0.27. The maximum biaxial strains in these tests are between 0.1% and 0.15% strain, present at the center of the square membrane. The peak-to-peak voltage signal (corresponding to the voltage which develops from 0 applied strain to the maximum out-of-plane deflection) is linearly related to the biaxial strain, as shown in Fig. 3. This

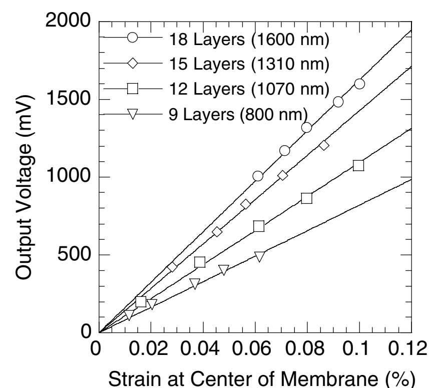

Fig. 3. Peak-to peak open-circuit piezoelectric membrane output versus membrane strain.

allows a calculation of the specific field generated, effectively the slope of Fig. 3.

There are several things to note regarding this measurement. Since the electrode is square and covers about 60% of the membrane area, the strain is not constant over the electrode. Normalizing by the maximum biaxial strain will create a lower bound estimate for the specific field. Additionally, since the external electrical contact is over the bulk silicon, the total capacitance of the system will be different than the capacitance over the region being strained. Since the structures are consistent between samples the linear relationship with strain and thickness allows normalized specific output to be used to compare device performance in terms of volts per percent strain per thickness of PZT (V/% ε μm PZT). The data in Fig. 3 indicate that the proportionality constant relating open-circuit voltage, PZT thickness and strain for present piezoelectric membranes is approximately 1 V for every micron thickness of PZT undergoing a biaxial strain of 0.1%.

The chemistry of the PZT, specifically the ratio of Zr to Ti, can have a substantial impact on the specific output (V/% ε μm PZT). A higher specific voltage translates to a higher voltage output from a membrane at a given strain. Since power increases as the square of the voltage, tailoring the specific output is very important to optimizing power output from the piezoelectric membrane.

The effects of PZT thickness and chemistry on power output from a 3 mm membrane are shown in Fig. 4. All three piezoelectric membranes were driven with the same pressure and frequency. Power is greatest from the 30 layer, 40:60 PZT membrane at a load resistance of 15 kΩ. The maximum power obtained from the 21 layer, 40:60 PZT was approximately equal to that from the 30 layer, 52:48 PZT at load resistances of 10 and 8 kΩ, respectively.

Measurements of charge based piezoelectric coefficients can be either based on applied stresses (d), or strains (e). As the measurements in this study are dynamic and only the field was directly measured (not the charge), we relate the field based piezoelectric coefficient, h_{31}, to the effective strain based piezoelectric coefficient for charge, e_{31}. In testing cantilevers, the electric displacement in the 3 direction, D_3, is related to the strains in the lateral directions 1 and 2 by

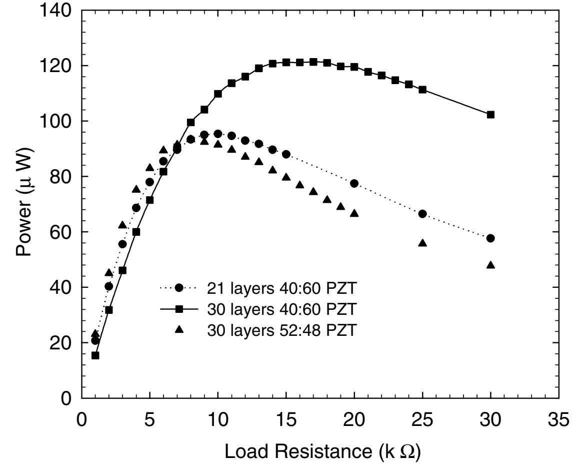

Fig. 4. Effect of PZT thickness and chemistry on piezoelectric membrane voltage output.

$$D_3 = e_{31}(S_1 + S_2). \quad (2)$$

As the maximum strain in the square membranes is biaxial, the strains in the 1 and 2 direction are equal. In the way d_{31} and g_{31} can be related though the dielectric constant ε^T (using the relative permittivity multiplied by the permittivity of free space, 8.85×10^{-12} F/m^2):

$$g_{31} = \frac{d_{31}}{\varepsilon^T}, \quad (3)$$

the specific field measured can be multiplied by the dielectric constant

$$e_{31} = h_{31}\varepsilon^T \quad (4)$$

to estimate a lower bound value of e_{31}. Therefore, the slope of Fig. 3, when divided by two and multiplied by the dielectric constant, is a lower bound estimate of e_{31}. It should be emphasized that the lower bound nature of this value is due to the non-uniform strain applied to the membrane, and not due to approximations of the elastic constants of the material (which are not required for strain based piezoelectric constants). This lower bound estimate of e_{31} is shown in Fig. 5 for 1 μm thick PZT films of various Ti concentrations. The peak e_{31} value is near the morphotropic phase boundary. However, the power generation from the 40:60 films is greater than that near the morphotropic phase boundary. This is likely due to the

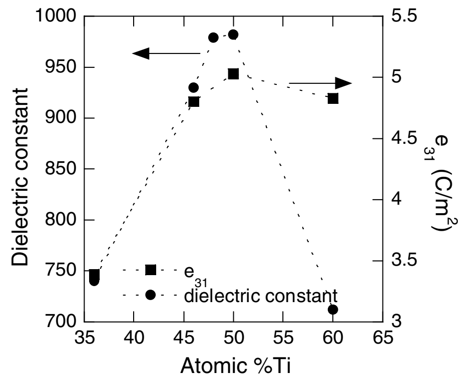

Fig. 5. Effect of Ti ratio on ε and e_{31}.

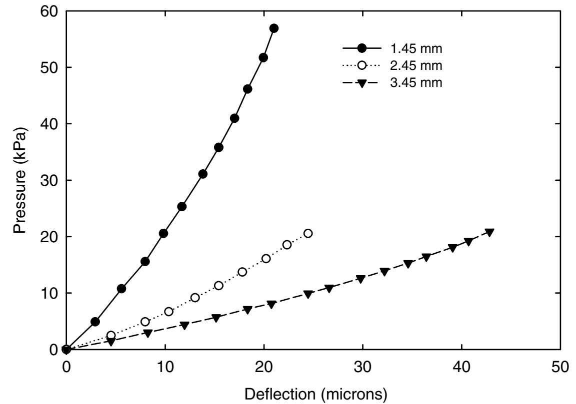

Fig. 6. Static deflection of a thin-film piezoelectric membrane versus applied pressure.

relationship for the figure of merit for power generation (FOM), which is directly related to the square of e_{31} and inversely related to the dielectric constant for films with a similar loss tangent ($\tan\delta$) as defined by Dubois and Muralt [13]:

$$\mathrm{FOM} = \frac{(e_{31})^2}{\varepsilon^{\mathrm{T}} \tan\delta}. \qquad (5)$$

As shown in Fig. 5, although e_{31} values for the 52:48 and 40:60 PZT films are similar, the dielectric constant decreases with increasing Ti ratio. Both the crystal structure and orientation contribute to this effect [14]. Power generation from tetragonal films (40:60 PZT) can be greater than those at the morphotropic phase boundary (52:48 PZT) with rhombohedral structure.

These results show that the strain, PZT thickness, and PZT chemistry are important to the design of a thin-film PZT membrane for power production applications. In order for a piezoelectric membrane generator to produce power for most realistic applications, the generator must operate for long durations and the membrane must flex many times without fracture or failure.

3.2. Experimental characterization of mechanical behavior

The mechanical behavior of typical piezoelectric membranes is seen in Fig. 6. Measurements for 1.45, 2.45 and 3.45 mm side length square piezoelectric membranes are plotted in terms of pressure versus membrane deflection. The pressure–deflection data can be converted to force–deflection data by multiplying the pressure on the membrane by the surface area of the membrane. The data collapse to yield a consistent spring constant of $k = 4700$ N/m, for membrane deflections up to 12 μm.

With operating frequencies expected to be in the range of 0.1–10 kHz, piezoelectric membrane lifetimes of greater than 10^8–10^{10} cycles are required. To assess device lifetimes and to characterize the reliability of the present generation of piezoelectric membranes, mechanical fatigue tests were undertaken.

Fig. 7 shows the results of one fatigue test in which a piezoelectric membrane has been deflected with maximum strain of 0.05%, for 10^8 cycles on the bulge tester. In the figure, the static deflection of a 1.45 mm square, 2.5 μm thick (2.0 μm silicon, 0.5 μm PZT) piezoelectric membrane is plotted as a function of pressure. Three pressure–deflection curves are given. The first curve was measured before the piezoelectric membrane was cycled. The second and third curves were measured after the piezoelectric membrane had been fatigued by driving it at 700 Hz with a 27 kPa pressure wave for 5.2×10^7 and 10^8 cycles, respectively. A small increase in compliance from the initial test is seen in the piezoelectric membrane after 5.2×10^7 cycles. However, subsequent cycling up to 10^8 cycles causes no further increase in compliance. The increase in compliance after 5.2×10^7 cycles is

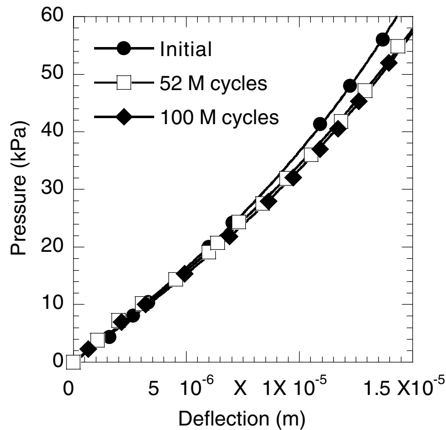

Fig. 7. Pressure versus deflection curves for a piezoelectric membrane after 0, 52×10^6, and 100×10^6 cycles.

postulated to be due to the appearance of microcracks in the membrane. Further fatiguing the piezoelectric membrane to 10^8 cycles apparently does not lead to growth of those microcracks.

The fracture mechanism in the composite structures was investigated under both static and dynamic loading. Static pressure to failure measurements showed a maximum strain at failure of 0.12%. Etching of the PZT layer to relieve high strain locations resulted in an increase of 40% in the static strain at failure. Fig. 8 shows the exposed Pt bottom electrode where the PZT was removed from the four high strain regions. The edges of the membrane lie half the distance between the parallel sides of the exposed Pt area. With this etched pattern we have not observed any evidence of fatigue cracking through 10^8 cycles.

Residual stresses within the membrane generator affect many aspects of generator performance including compliance, strain at failure and resonance frequency. The residual stress induced during processing has been characterized using X-ray diffraction, wafer curvature, and bulge-testing [15]. Residual stresses arise during processing and are primarily due to volume loss and thermal expansion mismatch during pyrolysis and crystallization fabrication steps. The magnitude of the residual stress in the resulting composite membrane structure is tensile and depends on many factors including PZT chemistry and thickness. Modest changes to the residual stress occur with the Zr:Ti

Fig. 8. Photograph of thin-film PZT membrane generator. Arrow denotes one of the four high strain regions.

ratio. The residual stress measured on a 3 mm side length membrane with 2 μm of Si and 1 μm of 52:48 PZT was 151 MPa compared to 101 MPa on a membrane composed of 40:60 PZT and identical geometric parameters. Pressure deflection data for these two membranes are shown in Fig. 9. Because of lower stresses in the silicon support structure, the composite residual stress is not linearly related to the PZT film thickness. In general, the stress in the PZT film will remain constant as thickness varies. The applied strain at failure depends upon the magnitude of residual stress, as shown in Fig. 10, where increasing the magnitude of the residual stress decreased the strain at failure of the membranes.

These results show that the multilayered structure comprising the thin-film PZT membrane generator has complex properties and behaviors which must be understood and modeled in order to optimize the design of the PZT membrane generators.

3.3. Modeling of mechanical behavior

There are many challenges in developing a model of this system; the structure is multilayered, there are residual stresses, deflections are large relative to the membrane thickness resulting in nonlinear behavior, there is coupling between bending and stretching, and there is electromechanical coupling.

In this work a static analysis is performed as a first step to elucidate the characteristics of the

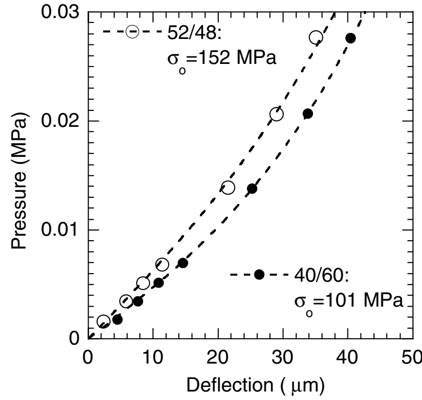

Fig. 9. Effect of PZT chemistry on membrane residual stress.

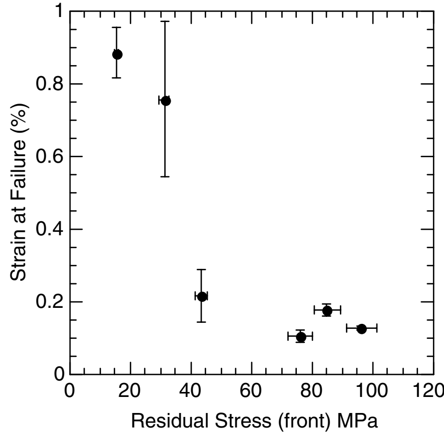

Fig. 10. Effect of residual stress on applied strain at failure.

structure and material properties. A variational approach is used to find the approximate closed form solution of the displacement field based on energy minimization.

The starting point is *Hamilton's principle* [16],

$$\delta \int_{t_0}^{t} L\,\mathrm{d}t + \int_{t_0}^{t} \delta W\,\mathrm{d}t = 0, \tag{6}$$

where W represents the work done by the external and body forces and the Lagrangian is

$$L = \int_V (T - H)\mathrm{d}V. \tag{7}$$

The first term is the Lagrangian, T, is the kinetic energy, H is electrical enthalpy density, and V is the volume. For static analysis at this stage the kinetic energy term is dropped. When electrical coupling is ignored and the applied electrical field is zero, the electrical enthalpy density becomes the strain energy density function U. This creates a simplified form of Eq. (6). It is a classical application of *the principle of virtual work* that can be stated as

$$\delta\Pi = \delta \int_V U\,\mathrm{d}V - \delta \int_A W\,\mathrm{d}A = 0, \tag{8}$$

where $U = \frac{1}{2}\sigma_{ij}\varepsilon_{ij}$ and σ_{ij} and ε_{ij} are the stress and strain tensors, respectively. Because of geometric non-linearity Von-Karman plate theory [16] assumptions are used for the strains. If u, v and w are in-plane deflections and the lateral deflection of the middle surface, and A is the surface area of the membrane, the contributions of the bending and membrane stretching to the internal strain energy is expressed as

$$U_{\text{bending}} = \frac{D}{2} \int_A \Big[(w_{,xx} + w_{,yy})^2 - 2(1-v)(w_{,xx}\,w_{,yy} - w_{,xy}^2) \Big] \mathrm{d}A, \tag{9}$$

$$U_{\text{membrane}} = \frac{Et}{2(1-v^2)} \int_A \Bigg(u_{,x}^2 + u_{,x}\,w_{,x}^2 + v_{,y}^2 + v_{,y}\,w_{,y}^2 + \left(\frac{w_{,x}^2 + w_{,y}^2}{2}\right)^2 + 2v\Big(u_{,x}\,v_{,y} + \frac{1}{2} v_{,y}\,w_{,x}^2 + \frac{1}{2} u_{,x}\,w_{,y}^2 \Big) + \frac{1-v}{2}\Big(u_{,y}^2 + 2u_{,y}\,v_{,x} + v_{,x}^2 + 2u_{,y}\,w_{,x}\,w_{,y} + 2v_{,x}\,w_{,x}\,w_{,y} \Big) \Bigg) \mathrm{d}A.$$

The second term in the virtual work expression is composed of two parts, namely the contribution of surface pressure, p, and the contribution of residual stresses, σ_0, generated during the manufacturing process.

$$W_p = \int_A pw\,\mathrm{d}A, \tag{10}$$

$$W_{\text{residual}} = -\int_A \left[\sigma_0 t \left(u_{,x} + \frac{1}{2} w_{,x}^2 + v_{,y} + \frac{1}{2} w_{,y}^2 \right) - m_0 (w_{,xx} + w_{,yy}) \right] \mathrm{d}A,$$

where σ_0 is the in-plane residual stress that is assumed to be uniform biaxial without shear, and m_0 is the bending moment caused by residual stresses.

When (9) and (10) are substituted in the total potential energy (Π) and the first variation is written as done in (8), it will produce a set of nonlinear partial differential equations that are the equilibrium equations for arbitrary virtual displacement increments. The finite difference method can be used for the solution of these equations. A predictor corrector type of approach is suitable to linearize the equations and to proceed with the solution iteratively. When bending is ignored the expressions simplify, however, nonlinearity does not disappear. The approximate closed form solutions usually provide a better prospect for parameter sensitivity analysis. Therefore, the Ritz method is applied in energy minimization to produce an approximate closed form solution in the following form

$$\bar{u} = \sum_{i=1}^{n} a_i \phi_i(x, y), \quad \bar{v} = \sum_{i=1}^{n} b_i \Psi_i(x, y), \quad \bar{w} = \sum_{i=1}^{n} c_i \varphi_i(x, y), \tag{11}$$

where a_i, b_i, c_i are the constants to be determined and $\phi_i, \Psi_i, \varphi_i$ are approximate base functions that satisfy geometric boundary conditions. Substituting these approximate forms into the variational equation and minimizing it with respect to the unknown coefficients to generate nonlinear sets of equations in terms of a_i, b_i, c_i are the steps to be followed in the method. Simply supported boundary conditions were chosen for this problem. The choice of the approximate functions is crucial to the achieved accuracy of the solution. Trigonometric series [16],

$$u = c \sin \pi x \cos \pi y, \quad v = c \sin \pi y \cos \pi x, \quad w = w_0 \cos \pi x \cos \pi y, \tag{12}$$

polynomials [17],

$$u = x(1 - x^2)(1 - y^2) \sum_{n=0}^{i} \sum_{m=0}^{i} a_{2n,2m} x^{2n} y^{2m},$$
$$v = y(1 - x^2)(1 - y^2) \sum_{n=0}^{i} \sum_{m=0}^{i} b_{2n,2m} x^{2n} y^{2m}, \tag{13}$$
$$w = (1 - x^2)(1 - y^2) \sum_{n=0}^{i} \sum_{m=0}^{i} c_{2n,2m} x^{2n} y^{2m},$$

and a mixture of these two [18],

$$u(x, y) = \left[u_0 + u_1(x^2 + y^2) + u_2 x^2 y^2 \right] \sin \pi x \cos \pi y,$$
$$u(x, y) = \left[u_0 + u_1(x^2 + y^2) + u_2 x^2 y^2 \right] \sin \pi y \cos \pi x,$$
$$w(x, y) = \left(w_0 + w_1 \frac{x^2 + y^2}{a^2} + w_2 \frac{x^2 y^2}{a^2} \right) \cos \frac{\pi x}{a} \cos \frac{\pi y}{a} \tag{14}$$

have been applied in the literature. In the current analysis all of these approaches have been tried.

Profiles obtained using different approximate functions are compared to experimental data in Fig. 11. The simplified form of (11), that is

$$u = A \frac{x}{a^5} (a^2 - x^2)(a^2 - y^2),$$
$$v = A \frac{y}{a^5} (a^2 - x^2)(a^2 - y^2), \tag{15}$$
$$w = \frac{w_0}{a^4} (a^2 - x^2)(a^2 - y^2) \left(1 + \frac{R}{a^2} (x^2 + y^2) \right)$$

yields the best agreement with the experimental data, as seen in Fig. 11.

Material parameters such as elastic modulus and Poisson's ratio, as well as residual stresses are needed to apply energy minimization. These are obtained from the pressure mid-point deflection curve as shown in Fig. 11. A simple analysis shows that pressure mid-point deflection has the following form [17,18]

$$p = C_1 \frac{\sigma_0 t}{a^2} w_0 + C_2 \frac{E t^3}{a^4} w_0 + C_3 \frac{E t}{a^4 (1 - v)} w_0^3, \tag{16}$$

where p is the applied uniform pressure, w_0 is the mid-point deflection of the square membrane, t is the thickness, and E is elastic modulus. The

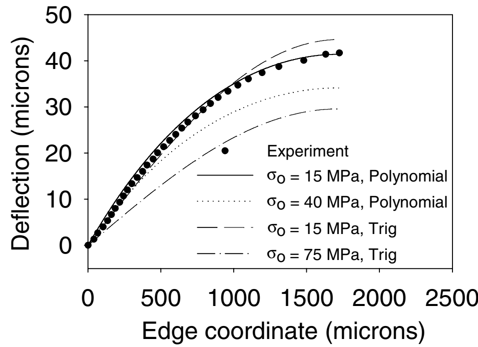

Fig. 11. Membrane profile along edge for experiment and different approximate forms in the energy minimization scheme.

residual bending moment at the edges is zero. The first term above shows the effect of the residual stresses, the second one shows the effect of bending and the third one is due to membrane stretching. As seen above the bending influence varies as the thickness cubed and so for small thicknesses has a negligible effect. Therefore, a cubic curve fit to the pressure mid-point deflection, like the one seen in Fig. 12, with an odd function which has a linear and a cubic term, will incorporate the effects of residual stress and membrane stretching. The coefficient C_1 can be obtained from the analytical solution of a harmonic equation for a transversely deflected membrane [16]. This calculation gives $C_1 = 3.393$. C_2 is reported in the literature [17] as a function of Poisson's ratio. Our analysis shows that $C_2 = 1.96 - 0.44v$. It is customary to use the bi-axial modulus $M = \frac{E}{1-v}$ instead of the elastic modulus. Once C_2 is obtained, the bi-axial modulus can be obtained from the cubic part of the curve fit. A single layer Si membrane can be used to obtain the bi-axial modulus for Si. The simple rule of mixtures is used for a multi-layer membrane, which, while not as accurate as the out of plane model [19], is used here as a first order approximation. Elastic moduli for Si $E_{Si} = 115$ GPa and for PZT $E = 70$ GPa are used. A composite Poisson's ratio of $v = 0.27$ is used in the calculations. Values obtained from different sets of experiments differ by only 10–15%.

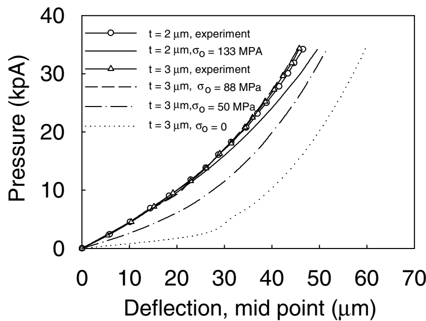

Fig. 12. Comparison of pressure–deflection curves obtained from experiments and energy minimization method for composite membranes of 2 and 3 μm thick.

The influence of the residual stresses can be seen in Figs. 13 and 14. Curve fits to the experimental data (Fig. 12) are used to obtain the residual stresses for multi layer membranes (composed of Si and PZT). It was found that $\sigma_0 = 88$ MPa for a 3 μm-thick membrane and $\sigma_0 = 133$ MPa for 2 μm-thick membrane. Fig. 12 shows that when the

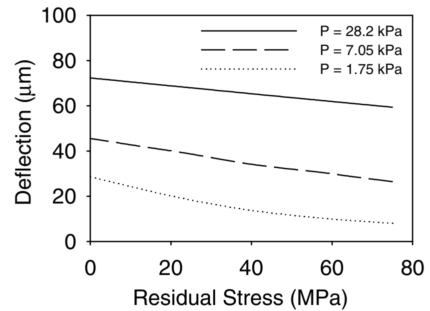

Fig. 13. Effect of residual stress on membrane deflection.

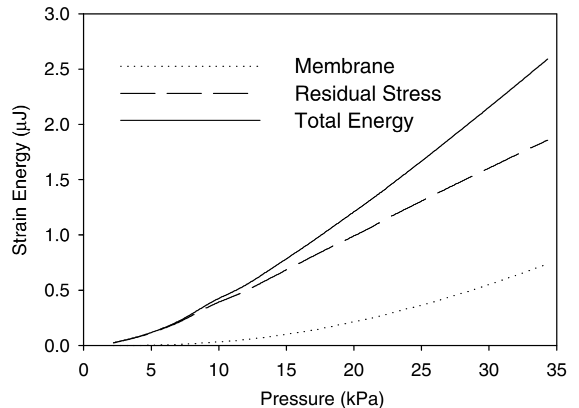

Fig. 14. Energy partition for residual stress and membrane stretching.

correct residual stress values obtained from the experiments are used in the Ritz method, theoretical curves are very close to the experimental ones. When the residual stress is changed, the coefficient of the cubic terms nearly remains constant proving that the cubic part is not influenced by the residual stresses. Fig. 13 shows the effect of the residual stresses on the membrane mid-point deflection. As the residual stresses increase the deflection for a given applied pressure decreases.

Another significant point examined is the partition of the total potential energy of the system. As discussed above bending, membrane stretching and residual stresses have an impact. The presence of residual stresses stiffen the structure and thus the portion of input energy required to deflect the membrane is increased. As seen in Fig. 14, the portion of the total energy required to offset the effects of residual stresses is much higher than that required for membrane stretching.

4. Conclusions

The behavior of thin-film PZT membranes operated at high deflections and strains has been studied. Pressure–deflection relationships, residual stresses, and electrical output characteristics of the piezoelectric membranes were acquired experimentally. A model was developed using an energy minimization technique and compared to the experimental results. The model was then used to explore the effects of residual stress.

The results indicate that it is critical to reduce and control the residual stress in the thin-film PZT membranes as much as possible. Experimental results have shown that increasing PZT thickness and the Ti ratio of the PZT chemistry lead to increased power output for a given deflection. The presence of residual stress in the composite structure can result in lower deflections for a given force and thus impact electrical output. Increasing the Ti ratio leads to a reduction in residual stress. Increasing PZT thickness has a small impact on composite residual stress. The total stress of the composite membrane is a weighted average of the individual layer stresses. Further reductions in residual stress may be achieved by depositing a compressive layer. This route will be investigated in future work.

Acknowledgements

Financial support was provided by DARPA MTO's MicroPower Generation Program and the US Army SMDC contract #DASG60-02-C0001. The SEM was performed at the Environmental Molecular Sciences Laboratory, a national scientific user facility sponsored by the Department of Energy's Office of Biological and Environmental Research and located at Pacific Northwest National Laboratory. The experimental assistance of James Raupp, Kevin Bruce, L.M.R. Eakins, B.W. Olson, and M.S. Kennedy is greatly appreciated.

References

[1] S. Whalen, M. Thompson, D. Bahr, C. Richards, R. Richards, Design fabrication and testing of the P3 micro heat engine, Sens. Actuators A 104 (2003) 200–208.
[2] R. Xu, S. Trolier-McKinstry, W. Ren, B. Xu, Z.-L. Xie, K.J. Hemker, J. Appl. Phys. 89 (2001) 1336–1348.
[3] D.L. Polla, L.F. Francis, Annu. Rev. Mater. Sci. 28 (1998) 563–597.
[4] J. Baborowski, N. Ledermann, P. Muralt, in: D.A. LaVan, A.A. Ayon, T.E. Buchheit, M.J. Madou (Eds.), Materials Research Society Symposium Proceedings, Nano- and Microelectromechanical Systems (NEMS and MEMS) and Molecular Machines, vol. 741, 2003, p. J12.4.1-6.
[5] R. Ballarini, Recent developments in experimental and theoretical studies of the mechanical behavior of polycrystalline silicon for microelectromecahnical systems, in: A.H. Heuer, S.J. Jacobs (Eds.), Materials Research Society Symposium Proceedings, Materials Science of MEMS Devices, vol. 546, 1999, pp. 3–14.
[6] X. Ding, W.H. Ko, J.H. Mansour, Sens. Actuators A 21–23 (1990) 866–871.
[7] D.F. Bahr, J.S. Robach, J.S. Wright, L.F. Francis, W.W. Gerberich, Mater. Sci. Eng. A 259 (1999) 126–131.
[8] D.F. Bahr, J.C. Merlino, P. Banerjee, C.M. Yip, A. Bandyopadhyay, Reliability and properties of PZT thin films for MEMS applications, in: A.H. Heuer, S.J. Jacobs (Eds.), Materials Research Society Symposium Proceedings, Materials Science of MEMS Devices, vol. 546, 1999, pp. 153–158.
[9] R.M. Cannon, B.J. Dalgleish, R.H. Dauskardt, T.S. Oh, R.O. Ritchie, Acta Metall. Mater. 39 (1991) 2145–2156.

[10] K.D. Budd, S.K. Dey, D.A. Payne, Br. Ceram. Proc. 36 (1985) 107–121.
[11] J.D. Hall, N.E. Apperson, B.T. Crozier, C. Xu, R.F. Richards, D.F. Bahr, C.D. Richards, Rev. Sci. Instr. 73 (2002) 2067–2072.
[12] J. Berstein, K. Houston, L. Niles, S. Finberg, H. Chen, L. Cross, K. Li, K. Udayakumar, Micromachined ferroelectric transducers for acoustic imaging, in: Proceedings of the 1997 International Conference on Solid State Sensors and Actuators, vol. 1, Chicago, IL, 1997, pp. 421–424.
[13] M.-A. Dubois, P. Muralt, Sens. Actuators 77 (1999) 106.
[14] L.M.R. Eakins, B.W. Olson, C.D. Richards, R.F. Richards, D.F. Bahr, J. Mater. Res. 18 (2003) 2079–2086.
[15] M.S. Kennedy, D.F. Bahr, C.D. Richards, R.F. Richards, Residual stress control to optimize PZT MEMS performance, in: David A. LaVan, Arturo A. Ayon, Thomas E. Buchheit, Marc J. Madou (Eds.), Proceedings of the Materials Research Society, Nano- and Microelectromechanical Systems (NEMS and MEMS) and Molecular Machines, vol. 741, 2003, p. J5.37.1–6.
[16] S.P. Timoshenko, S. Woinowsky-Krieger, Theory of Plates and Shells, McGraw Hill, New York, 1970.
[17] J.J. Vlassak, New Experimental Techniques and Analysis Methods for the Study of the Mechanical Properties of Materials in Small Volumes, Ph.D. Thesis, Stanford University, 1994.
[18] D.M. Schneider, J. Maibach, E. Obermeier, J. MEMS 4 (1995) 238–241.
[19] J.W. Hutchinson, Z. Suo, Adv. Appl. Mech. 29 (1992) 63–191.